

# Spiral Vortices and Taylor Vortices in the Annulus between Counter-rotating Cylinders

Christian Hoffmann and Manfred Lücke

Institut für Theoretische Physik,  
Universität des Saarlandes, D-66041 Saarbrücken, Germany

Ref: <b>Physics of Rotating Fluids</b> , <i>Lecture Notes in Physics, LNP 549</i> , edited by C. Egbers and G. Pfister (Springer, 2000), p. 55-66
--

**Abstract.** Vortices in the Taylor-Couette system with counter-rotating cylinders are investigated numerically in a set up with radius ratio  $\eta = 0.5$ . The full, time dependent Navier-Stokes equations are solved with a combination of a finite difference and a Galerkin method. Structure, dynamics, and bifurcation behavior of Taylor vortices and of spiral vortex solutions are elucidated. Some of their properties obtained for axially periodic boundary conditions are compared with recent experimental results.

## 1 Introduction

Vortex flow in the Taylor-Couette system with counter-rotating cylinders has attracted an ever increasing research interest since in 1966 Krueger et al. [1] predicted primary transitions to nonaxisymmetric rotating-wave flow, which then were observed in experiments by Snyder [2], who had presented experimental evidence for different types of stable helical flow (referred to as 'spirals') a few years earlier. In 1985 an experimental survey was published by Andereck et al. [3], which classified a large variety of different flow states, including some spiral types like linear, modulated, interpenetrating, and wavy spirals etc. An extensive numerical linear stability analysis was then performed for a wide range of radius ratios by Langford et al. [4]. At this time, Tagg et al. [5] experimentally observed a transition from the basic circular Couette flow (CCF) to axially standing and azimuthally traveling waves (ribbons) and found numerically calculated wave speeds to be in accord with experimental results. Edwards [6] studied the transition from CCF to traveling waves. A literature survey has been compiled by Tagg [7] and a review of the bifurcation theory can be found in ref. [8].

Recently Antonijoan et al. [9] presented an extensive numerical analysis of spiral flow in a system with a relatively narrow gap subject to axially periodic boundary conditions. They used a pseudospectral discretization of the Navier-Stokes equations (NSE) in a co-rotating frame of reference with helical coordinates which were adapted to the expected spiral pattern. In this contribution we present numerical results obtained with a finite differences algorithm combined with a Galerkin spectral code. The focus of our study is on comparing the spatio-temporal structure and the bifurcation behavior of Taylor Vortex Flow (TVF) and Spiral Vortex Flow (SPI) being competing primary vortex patterns that bifurcate out of the CCF basic state.

## 2 System

We report results obtained numerically for a Taylor-Couette system with counter-rotating cylinders. The ratio  $\eta = r_1/r_2$  of the radii  $r_1$  and  $r_2$  of the inner and outer cylinders was fixed at the value  $\eta = 0.5$  for which also experiments have been performed recently [10]. We consider the fluid in the annulus between the cylinders to be isothermal and incompressible with kinematic viscosity  $\nu$ . The gap width  $d = r_2 - r_1$  is used as the unit of length and the momentum diffusion time  $d^2/\nu$  radially across the gap as the time unit so that velocities are reduced by  $\nu/d$ . To characterize the driving of the system we use the Reynolds numbers

$$R_1 = r_1 \Omega_1 d / \nu ; R_2 = r_2 \Omega_2 d / \nu . \quad (1)$$

They are just the reduced azimuthal velocities of the fluid at the inner and outer cylinder, respectively, where  $\Omega_1$  and  $\Omega_2$  are the respective angular velocities. Within this scaling the Navier-Stokes equations (NSE) take the form

$$\partial_t \mathbf{u} = \nabla^2 \mathbf{u} - (\mathbf{u} \cdot \nabla) \mathbf{u} - \nabla p \quad (2)$$

with  $p$  denoting the pressure field that is reduced by  $\rho \nu^2 / d^2$  where  $\rho$  is the mass density of the fluid. Using cylindrical coordinates the velocity field

$$\mathbf{u} = u \mathbf{e}_r + v \mathbf{e}_\varphi + w \mathbf{e}_z \quad (3)$$

is decomposed into a radial component  $u$ , an azimuthal one  $v$ , and an axial one  $w$ . We have solved the resulting equations subject to no slip conditions at the cylinders. Axially we imposed periodic boundary conditions at  $z = 0$  and  $z = \Gamma$  where  $\Gamma$  is the reduced periodicity length. In this work we mostly considered  $\Gamma = 1.6$ . Then, the wave number of the TVF and the SPI was  $k = 2\pi/\Gamma = 3.927$ .

For the numerical calculations, we use a combination of a finite differences formulation in the  $r - z$  plane with a spectral decomposition in  $\varphi$ . Since we are studying also finite length cylinders with rigid lids closing the annulus vertically we do not use a code with an axial Fourier decomposition which for axially periodic systems would be an interesting alternative. The discretization (a FTCS - Forward Time, Centered Space algorithm) has been done on staggered grids in the  $r - z$  plane following the procedure of ref. [11]. In this way one obtains simple expressions for derivatives in  $r$  and  $z$  - especially when the derivative, e.g.,  $\partial_r$  of a field, e.g.,  $u$  has to be calculated in the balance equation of another field, e.g.,  $v$ . Furthermore, since  $u$ ,  $v$ , and  $w$  lie on different grids, we never have to impose boundary conditions for more than one velocity field component at the same position. Moreover, the pressure field does not require additional boundary conditions (cf. below). Mostly we used homogeneous grids with discretization lengths  $\Delta r = \Delta z = 0.05$  and time steps  $\Delta t < 1/3600$ .

To allow also nonaxisymmetric flow structures in our code, we expand all fields in azimuthal Fourier modes  $e^{im\varphi}$ , e.g.,

$$\mathbf{u}(r, \varphi, z, t) = \sum_{m=-m_{max}}^{m_{max}} \hat{\mathbf{u}}_m(r, z, t) e^{im\varphi} . \quad (4)$$

The pressure is expanded similarly. For the flows investigated here a truncation of the mode expansion at  $m_{max} = 8$  was sufficient to properly resolve the anharmonicities in the fields. Inserting these expansions into the NSE and projecting onto the respective normal modes  $e^{im\varphi}$  we obtain a system of coupled equations for the mode amplitudes  $\hat{\mathbf{u}}_m(r, z, t)$  that is solved with the FTCS algorithm. To that end all modes  $-m_{max} \leq m \leq m_{max}$  have to be evaluated at time  $t$  before any mode can be calculated at the next timestep  $t + \Delta t$ . Having stepped up the velocity field with the FTCS algorithm the pressure  $p$  is determined with the method of 'artificial compressibility' [12]

$$dp^{(n)} = -\beta \nabla \cdot \mathbf{u}^{(n)} \quad (0 < \beta < 1) \quad (5)$$

$$p^{(n+1)} = p^{(n)} + dp^{(n)} \quad (6)$$

$$\mathbf{u}^{(n+1)} = \mathbf{u}^{(n)} - \Delta t \nabla (dp^{(n)}). \quad (7)$$

With this relaxation method pressure and velocity fields are iteratively adjusted to each other. The pressure correction  $dp^{(n)}$  in the  $n$ -th iteration step is proportional to the divergence of  $\mathbf{u}$ , which should be zero in the relaxed case, satisfying the continuity equation. The corrected pressure is then used to adapt the velocity field. The iteration loop (5-7) is executed for each azimuthal Fourier mode separately. It is iterated until  $\nabla \cdot \mathbf{u}$  has become sufficiently small for each  $m$  mode considered. After that the next FTCS time step is executed.

### 3 Linear stability analysis of CCF

We have also performed a linear stability analysis of the basic CCF state using a shooting algorithm with a fourth order Runge-Kutta integration method. Fig. 1 shows for  $R_2 = -100$  as a representative example the marginal stability thresholds  $R_{1,stab}$  of the CCF state against perturbations with axial wave number  $k$  and azimuthal wave number  $M = 0, 1, 2$ , respectively. Note that these curves in the  $k - R_1$  plane of Fig. 1 are bifurcation thresholds for rotationally symmetric TVF ( $M = 0$ ) and SPI ( $M = 1, 2$ ) solutions, respectively. The linear analysis shows that for wave numbers  $k > 5.1$  the  $M = 0$  instability to TVF occurs first when increasing  $R_1$ . For  $k < 5.1$ , however, first a spiral solution with azimuthal wave number  $M = 1$  bifurcates out of the CCF state when increasing  $R_1$  while  $M = 0$  perturbations can grow only at larger  $R_1$ . The marginal stability thresholds for perturbations with  $M \geq 2$  lie substantially above those for  $M = 0$  and  $M = 1$  perturbations.

Note that the wave number  $k = 2\pi/1.6 = 3.927$  for which we have explored nonlinear TVF and SPI states is close to the critical ones for  $M = 0$  and  $M = 1$  perturbations. This does not hold only for  $R_2 = -100$  but also for the wide range of  $R_2$ -values covered in Fig. 2: the marginal stability thresholds  $R_{1,stab}$  plotted in Fig. 2a versus  $R_2$  are very similar to the corresponding critical ones,  $R_{1,c}$ , shown in Fig. 2b. For completeness, we show in Fig. 2c the critical axial wave numbers for  $M = 0, 1, 2$  perturbations and in Fig. 2d the critical frequencies  $\omega_c/M$  for  $M = 1, 2$ .

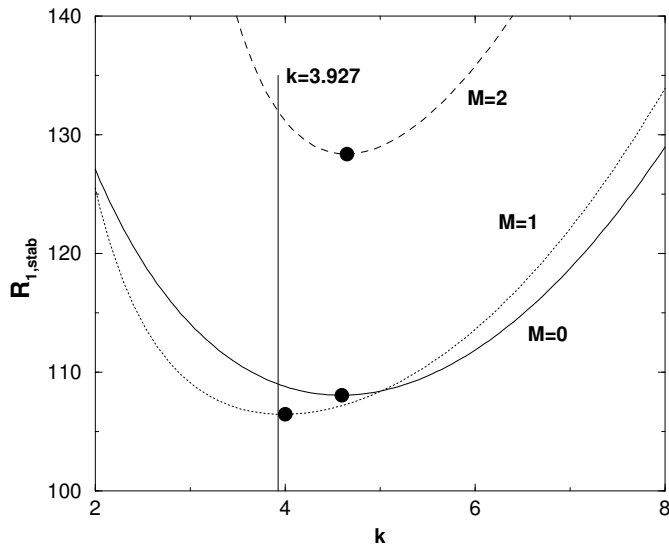


**Fig. 1.** Stability thresholds of the CCF basic state against perturbations with different azimuthal wave numbers  $M$  as indicated. Marginal stability curves  $R_{1,stab}$  are shown versus axial wave number  $k$ . Points denote the critical values. Parameters are  $\eta = 0.5$ ,  $R_2 = -100$ .

#### 4 Bifurcation properties of Taylor vortex and spiral flow

Here we present results concerning the bifurcation behavior of the  $M = 0$  TVF and of SPI solutions with azimuthal wave number  $M = 1$  as functions of the inner cylinder's Reynolds number  $R_1$ . We have not tried to locate and investigate the  $M = 2$  SPI solution. Parameters are fixed in this section at  $\eta = 0.5$ ,  $R_2 = -100$ , and the axial periodicity length is  $L = 1.6$ . In order to display the structural differences between TVF and SPI flow we show in Fig. 3a for both patterns the velocity field in the  $r - z$  plane and in Fig. 3b the velocity field in the cylindrical  $\varphi - z$  plane at mid gap,  $r_1 + 0.5$ .

Fig. 4a shows the bifurcation diagrams of maximal radial flow velocity versus  $R_1$  for  $M = 1$  SPI (lozenges) and for TVF (circles). Both flow states bifurcate supercritically out of the basic CCF state. The numerical bifurcation thresholds lie slightly below the respective ones,  $R_{1,stab}(M = 1) = 106.4551$  and  $R_{1,stab}(M = 0) = 108.9988$ , obtained in Sec. 3 within the linear stability analysis due to the discretization errors of the FTCS numerical code. The SPI solution is stable throughout the driving range shown in Fig. 4. Beyond it the SPI state loses stability to a more complicated time dependent pattern that we shall not discuss here. TVF, on the other hand is unstable (open circles) close to onset, becomes stable between  $R_1 = 120$  and  $R_1 = 125$ , and finally

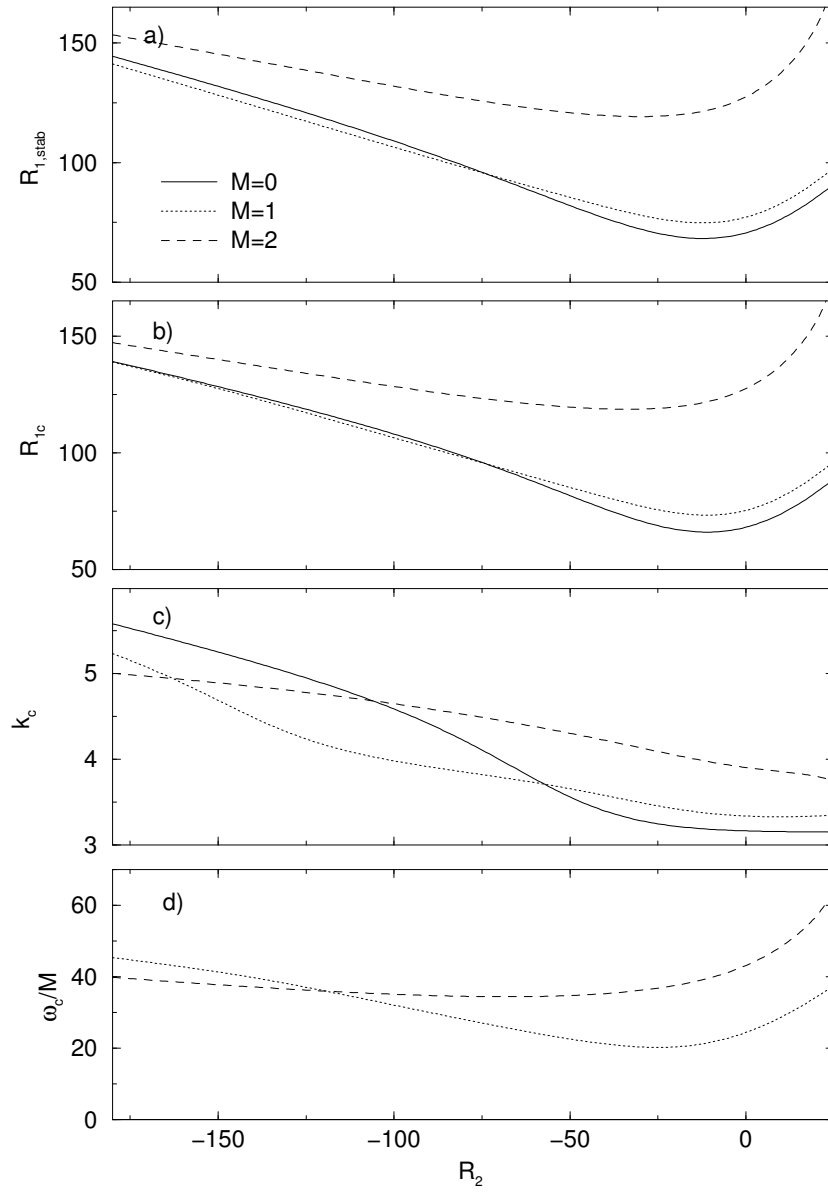


**Fig. 2.** Results of a linear stability analysis of the CCF basic state for  $\eta = 0.5$  as functions of  $R_2$  for perturbations with different azimuthal wave numbers  $M$  as indicated: (a) stability threshold  $R_{1,stab}$  for axial wave number  $k = 3.927$ , (b) critical Reynolds number  $R_{1,c}$ , (c) critical axial wave number  $k_c$ , (d) critical frequency  $\omega_c/M$ .

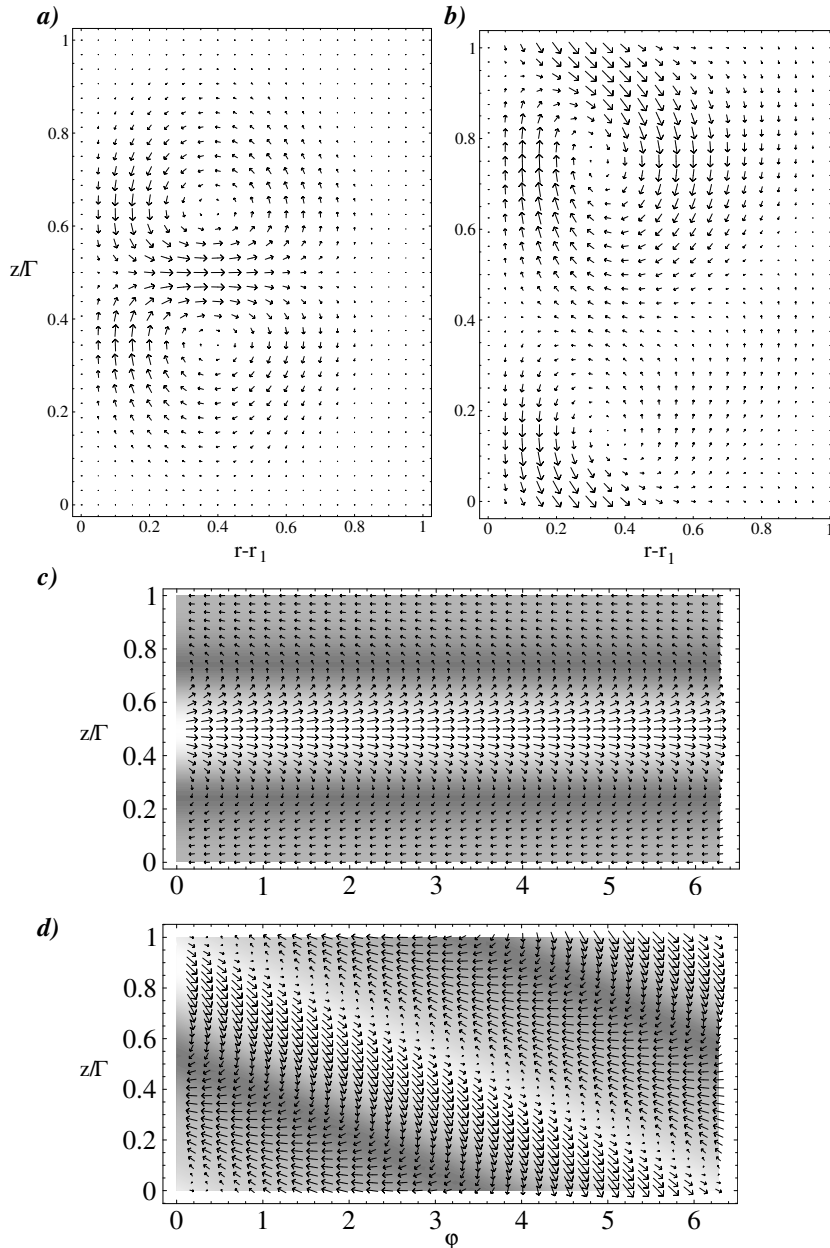


**Fig. 3.** Structure of TVF and of a left handed SPI state with axial wave number  $M = 1$ . Snapshots of the velocity field  $u\mathbf{e}_r + w\mathbf{e}_z$  in the  $r - z$  plane are shown in (a) for TVF and in (b) for SPI. The field  $v\mathbf{e}_\varphi + w\mathbf{e}_z$  in the cylindrical  $\varphi - z$  plane at mid gap,  $r_1 + 0.5$ , is shown in (c) for TVF and in (d) for SPI together with a grey scale plot of  $u$  with dark grey denoting maximal radial inflow and light grey denoting maximal radial outflow, respectively. See Fig. 6 for axial profiles of  $u$  and section 5 for a discussion of the fact that Taylor vortices appear more compressed than spiral vortices. Parameters are  $\eta = 0.5$ ,  $\Gamma = 1.6$ ,  $k = 3.927$ ,  $R_1 = 140$ , and  $R_2 = -100$ .

loses stability around  $R_1 \simeq 150$ . Here stability of the rotationally symmetric TVF solution refers to the situation covered by our code that allows the development of  $M \neq 0$  perturbations which break the rotational symmetry of TVF. The unstable TVF solution (open circles) close to onset was obtained by discarding any azimuthal mode with  $m \neq 0$ , thus enforcing rotational symmetry. The TVF solution marked by open circles is stable against  $M = 0$  but unstable against  $M \neq 0$  perturbations with the prescribed axial periodicity of  $\Gamma = 1.6$ . Beyond the last filled circle at  $R_1 \simeq 150$  in Fig. 4 the TVF state loses stability even in the  $M = 0$  subspace against a time dependent state that we shall not discuss here further. We have not determined the TVF solution that is unstable in the  $M = 0$  subspace beyond  $R_1 \simeq 150$  since this requires a different procedure. Therefore our TVF solution branch ends in Fig. 4 at  $R_1 \simeq 150$ .

So, in the driving range  $125 \leq R_1 \leq 150$  we found in our axially periodic system bistability between TVF and SPI. At the low driving end,  $R_1 \lesssim 125$ , of the stability range of TVF the system undergoes a transition to a stable  $M = 1$  SPI flow. On the other hand, when increasing  $R_1$  beyond the high driving stability boundary of TVF at  $R_1 \gtrsim 150$  the Taylor vortices typically develop an oscillatory time dependence.

It is instructive to compare our numerically obtained bifurcation behavior of TVF and SPI with recent experiments for  $\eta = 0.5$  despite the fact that they were done in a relative short system of length  $\Gamma = 12$  with rigid, stationary end plates closing the annulus [10]. For  $R_2 = -96.69$  being close to our value of  $R_2 = -100$  the authors observed  $M = 1$  SPI flow in the center part of the system with axial wave number  $k = 3.57$  which differs somewhat from our  $k = 3.927$ . However, this SPI flow was seen only in the driving range  $106 \lesssim R_1 \lesssim 118$ . Beyond  $R_1 \simeq 118$  the SPI flow underwent a transition into stable TVF. This TVF state lost its stability to wavy vortex flow at a driving value of  $R_1 \simeq 168$  that lies above the upper stability boundary for TVF,  $R_1 \gtrsim 150$ , in our axially periodic system. The significant downwards (upwards) shift in the *upper* stability boundary of experimental SPI (TVF) compared to the axially periodic numerical result is presumably related to the fact that the rigid end plates with adjacent stationary, rotationally symmetric Ekman vortices suppressing axial phase propagation tend to destabilize SPI and stabilize TVF. This stabilizing effect on TVF is presumably also responsible for the downwards extension of experimental TVF down to  $R_1 \simeq 118$ , i.e., below the *lower* stability boundary of TVF under axially periodic boundary conditions at  $R_1 \lesssim 125$ .

In Fig. 5a we show the bifurcation diagrams of the axial mean flow  $\langle w \rangle$  of our spiral states shown in Fig. 4. And Fig. 5b displays the axial phase velocities  $w_{ph}$  of the spirals versus  $R_1$ . The open lozenges therein refer to the experimental results for the phase velocity [10]. For our SPI states the axial mean flow (i.e.  $w$  integrated over the annular cross section at a fixed  $z$ ) is independent of  $z$  and  $t$  since all spiral fields

$$f_{\text{SPI}}(r, \varphi, z, t) = F_{\text{SPI}}(r, \phi)$$

depend only via the phase variable  $\phi = kz + M\varphi - \omega t$  on  $\varphi$ ,  $z$  and  $t$ .

While for our periodic boundary conditions, Reynolds stresses of the SPI velocity field generate a finite  $\langle w \rangle$  the rigid end plates of the experimental set up suppress any axial net flow  $\langle w \rangle$ . However, it should be noted that the difference between experimental and numerical axial phase velocities cannot be explained by  $w_{ph} - \langle w \rangle$ . For the spirals discussed here  $\langle w \rangle$  is directed opposite to the axial phase velocity,  $w_{ph}$ .

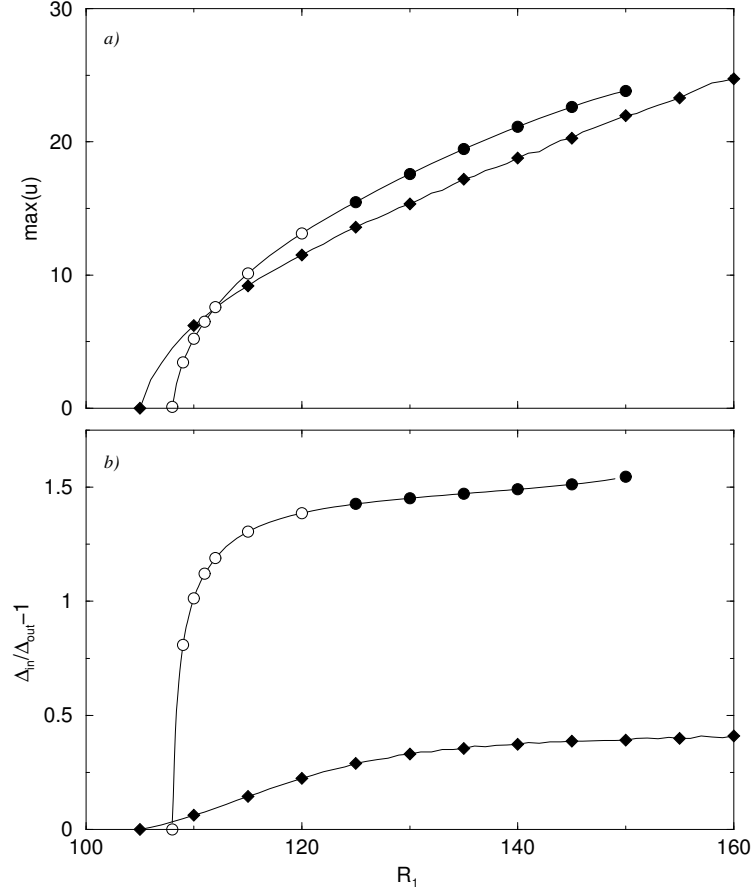


**Fig. 4.** Bifurcation diagrams of  $M = 1$  SPI (lozenges) and TVF (circles) order parameters versus  $R_1$ . Filled (open) symbols refer to stable (unstable) solutions; see text for further explanations. (a) maximal radial flow velocity, (b) inflow/outflow asymmetry measured by the ratio of axial ranges  $\Delta_{in}$  ( $\Delta_{out}$ ) of radial inflow (outflow) in the middle of the gap. Parameters are  $\eta = 0.5$ ,  $k = 3.927$ ,  $R_2 = -100$ .

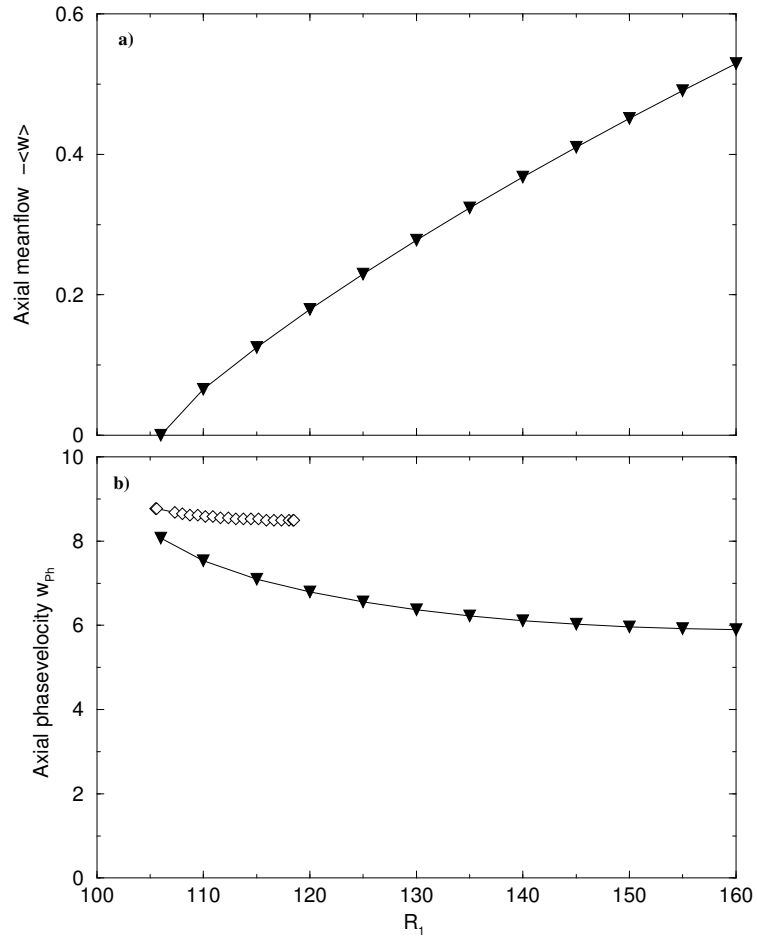


**Fig. 5.** Axial mean flow (a) and phase velocity (b) of left handed SPI states with azimuthal wave number  $M = 1$  versus  $R_1$ . Filled triangles show results from our simulations with axially periodic boundary conditions. Open lozenges are experimental results [10]; see text for further explanations. Simulation parameters were  $\eta = 0.5$ ,  $k = 3.927$ , and  $R_2 = -100$ .

## 5 Structure of Taylor vortex and spiral flow

Spirals bifurcate out of the CCF state in a Hopf bifurcation. They break the rotational symmetry, the axial mirror symmetry, the axial translational invariance, and the time translational invariance of the NSE. Their spatio temporal structure in  $\varphi, z, t$  depending only on the combined phase  $\phi = kz + M\varphi - \omega t$  is effectively one dimensional.

All spirals reported here rotate in positive  $\varphi$  direction. Depending on initial conditions, the flow either evolved into a right handed spiral (R-SPI) or into a left handed (L-SPI) being the mirror image of an R-SPI under the operation  $z \rightarrow -z$  of axial inversion. The rotation in positive  $\varphi$  direction implies for the R-SPI (L-SPI) an axial translation of the phase with negative (positive) phase velocity  $w_{ph}$ . At onset  $w_{ph}$  agrees within the numerical accuracy of our code with the phase velocity  $\omega/k$  resulting from the linear stability analysis.

Finally we want to discuss the axial structure of TVF and of spiral flow. To that end we show in Fig. 6 how the axial profile of the radial velocity  $u$  at mid gap position evolves with  $R_1$ . Here, positive (negative)  $u$  implies radial outflow (inflow). First one observes that the mirror symmetry of the TVF profiles in Fig. 6a around the position,  $z = 0.5$ , of maximal radial outflow is broken in the spiral waves that are propagating in Fig. 6b to the right. The axial wave profiles of these travelling SPI states become more and more anharmonic as  $R_1$  increases such that the waves become steeper before (flatter behind) the crests. Measuring the axial anharmonicity of the vortex structures by the difference of the axial ranges of radial inflow and outflow,  $\Delta_{in}$  and  $\Delta_{out}$ , respectively, one sees that TVF is much more anharmonic than SPI flow. This is also corroborated by a direct axial Fourier analysis of  $u$ . The bifurcation behavior of  $\Delta_{in}/\Delta_{out} - 1$  is shown in Fig. 4b. This quantity measures the anharmonicity of  $u$  via the asymmetry in the inflow/outflow ranges and also – because of the continuity constraint – the asymmetry of the respective radial flow amplitudes. Thus, Taylor vortices appear to be smaller in size than spiral vortices that seem to fill almost the whole gap in Fig. 3.

## 6 Summary

For a counter-rotating system with radius ratio  $\eta = 0.5$  we have numerically determined the spatio temporal properties and the bifurcation behavior of TVF and of  $M = 1$  SPI states that bifurcate with increasing  $R_1$  supercritically out of the basic CCF. We investigated in particular outer cylinder Reynolds numbers  $R_2$  where the bifurcation to stable SPI occurs first and the bifurcation to initially unstable TVF is located at a higher value of the inner cylinder Reynolds number  $R_1$ . For axially periodic boundary conditions SPI remained stable for a wide range of  $R_1$  while the TVF solution becomes stable slightly above onset. Thus, there is a substantial range of  $R_1$  with bistable coexistence and competition of TVF and of the two mirror symmetry degenerated L-SPI and R-SPI states with left handed and right handed spiral vortices, respectively. In the parameter range investigated here the two latter rotate both in positive  $\varphi$  direction so that the axial phase velocity  $w_{ph}$  of the L-SPI (R-SPI) wave is positive (negative). The axial mean flow generated by the SPI wave is directed opposite to  $w_{ph}$ . Typically spiral vortices are for our  $\eta = 0.5$  less anharmonic than Taylor vortices. A comparison with recent experimental results suggests that rigid endplates tend to reduce (enlarge) the stability range of SPI (TVF).

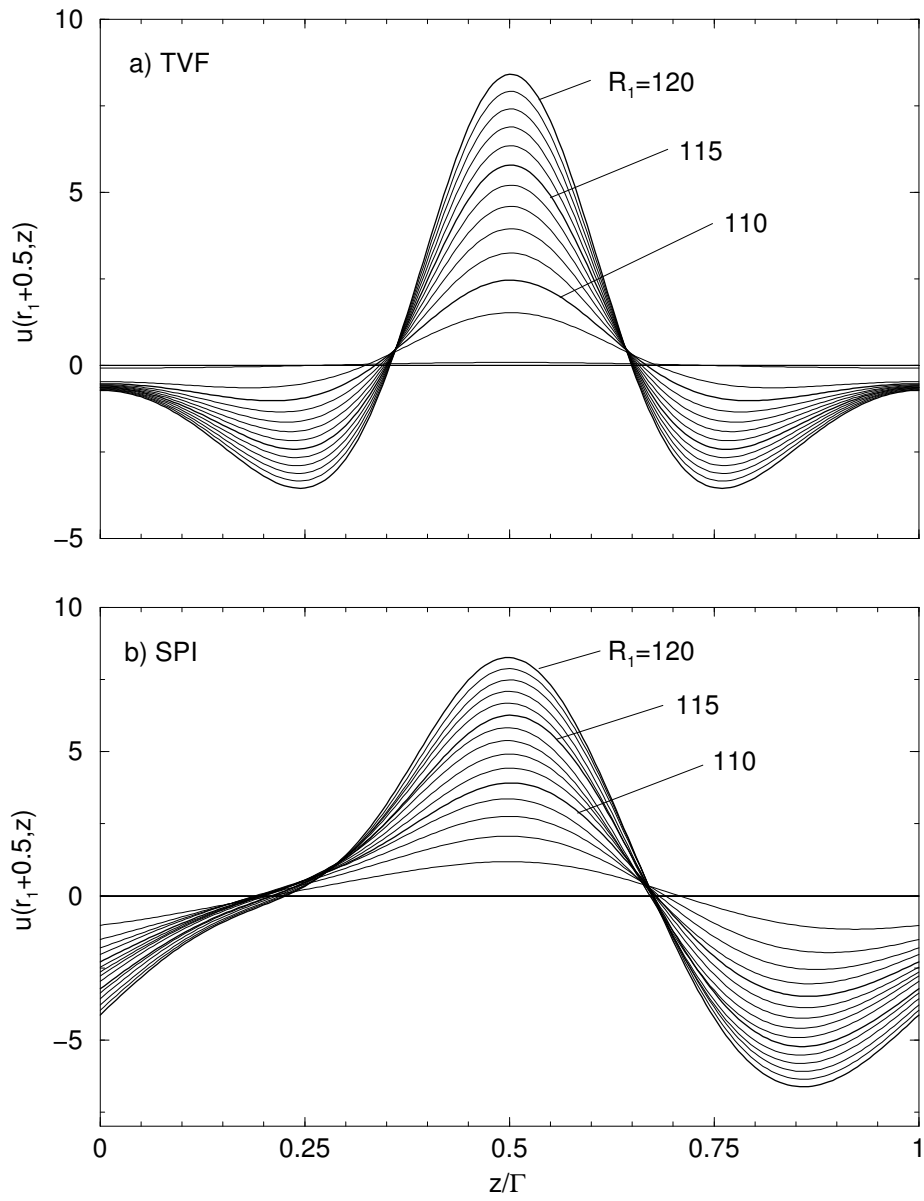


**Fig. 6.** Axial profiles of the radial velocity field at mid gap location for TVF (a) and L-SPI (b) with azimuthal wave number  $M = 1$ . The phase velocities in (b) are positive. Parameters are  $\eta = 0.5$ ,  $k = 3.927$ ,  $R_2 = -100$ , and  $R_1$  as indicated.

## Acknowledgments

We thank A. Schulz for communicating the experimental data referred to in this paper.

## References

1. E. R. Krueger, A. Gross, and R. C. DiPrima: *On the relative importance of Taylor-vortex and nonaxisymmetric modes in flow between rotating cylinders*, J. Fluid Mech. **24**, 521 (1966).
2. H. A. Snyder: *Stability of rotating Couette flow. I. Asymmetric waveforms*, Phys. Fluids **11**, 728 (1968).
3. C. D. Andereck, S. S. Liu, and H. L. Swinney: *Flow regimes in a circular Couette system with independently rotating cylinders*, J. Fluid Mech. **164**, 155 (1986).
4. W. F. Langford, R. Tagg, E. Kostelich, H. L. Swinney, and M. Golubitsky: *Primary instabilities and bicriticality in flow between counter-rotating cylinders*, Phys. Fluids, **31**, 776 (1988).
5. R. Tagg, W. S. Edwards, H. L. Swinney, and P. S. Marcus: *Nonlinear standing waves in Couette-Taylor flow*, Phys. Rev. A **39**, 3734 (1988).
6. W. S. Edwards: *Linear Spirals in the finite Couette-Taylor problem*, in *Instability and Transition, Vol. II*, edited by M. Y. Hussaini, (Springer-Verlag, Berlin, 1990), p. 408.
7. R. Tagg: *A Guide to literature related to the Taylor-Couette problem*, in *Ordered and Turbulent Patterns in Taylor-Couette Flow*, edited by C. D. Andereck and F. Hayot (Plenum, New York, 1992).
8. P. Chossat and G. Iooss: *The Couette-Taylor Problem*, (Springer-Verlag, Berlin, 1994).
9. J. Antonijoan, F. Marquès, and J. Sánchez: *Non-linear spirals in the Taylor-Couette problem*, Phys. Fluids **10** 4, 829 (1998).
10. A. Schulz and G. Pfister: contribution to this volume.
11. C. W. Hirt, B. D. Nichols, and N. C. Romero: *SOLA — A Numerical Solution Algorithm for Transient Fluid Flow*, (Los Alamos Scientific Laboratory of the University of California, LA-5852, 1975)
12. R. Peyret and T. D. Taylor: *Computational Methods in Fluid Flow*, (Springer-Verlag, Berlin, 1983).